Enhancing the resolution of micro free flow electrophoresis through spatially controlled sample injection

Journal:	*Analytical Chemistry*
Manuscript ID	ac-2018-012052.R2
Manuscript Type:	Article
Date Submitted by the Author:	21-Jun-2018
Complete List of Authors:	Saar, Kadi; University of Cambridge, Department of Chemistry Müller, Thomas; University of Cambridge, Department of Chemistry Charmet, Jerome; University of Warwick, WMG Challa, Pavan; University of Cambridge, Chemistry Knowles, Tuomas; University of Cambridge, Nanoscience Centre

Enhancing the resolution of micro free flow electrophoresis through spatially controlled sample injection

Kadi L. Saar,[†] Thomas Müller,[‡] Jérôme Charmet,[¶] Pavan Kumar Challa,[†] and Tuomas P.J. Knowles[*,†,§]

[†]*Department of Chemistry, University of Cambridge, Lensfield Road, Cambridge CB2 1EW, UK*

[‡]*Fluidic Analytics Limited, Unit 5 Chesterton Mill, French's Road, Cambridge CB4 3NP, UK*

[¶]*Institute of Digital Healthcare, WMG, University of Warwick, Coventry CV4 7AL, UK*

[§]*Cavendish Laboratory, Department of Physics, University of Cambridge, J J Thomson Ave, Cambridge CB3 0HE, UK*

E-mail: tpjk2@cam.ac.uk

Abstract

Free flow electrophoresis is a versatile technique for the continuous separation of mixtures with both preparative and analytical applications. Microscale versions of free flow electrophoresis are particularly attractive strategies because of their fast separation times, ability to work with small sample volumes and large surface area to volume ratios facilitating rapid heat transfer, thus minimising the detrimental effects of Joule heating even at high voltages. The resolution of microscale free flow electrophoresis, however, is limited by the broadening of the analyte beam in the microfluidic channel - an effect

that becomes especially pronounced when the analyte is deflected significantly away from its original position. Here we describe and demonstrate how restricting spatially the sample injection and collection to the regions where the gradients in the velocity distribution of the carrier medium are the smallest allows this broadening effect to be substantially suppressed and hence the resolution of microscale free flow electrophoresis devices to be increased. To demonstrate this concept, we fabricated microfluidic free flow electrophoresis devices with spatially restricted injection nozzles implemented through the use of multilayer soft-photolithography and further integrated quartz based observation areas for fluorescent detection and imaging. With these devices we demonstrated a five fold reduction in the extent of beam broadening relative to conventional free flow electrophoresis approaches with non-restricted sample introduction. The manifold enhancement in the achievable resolution of microscale free flow electrophoresis devices opens up the possibility of rapid separation and analysis of complex mixtures.

Introduction

Free flow electrophoresis is a powerful tool for the continuous separation and analysis of mixtures.[1–9] In free flow electrophoresis systems a sample stream is surrounded by carrier medium and exposed to an electric field applied perpendicularly to the direction of flow which enables continuous separation of the components in the mixture according to their charge to hydrodynamic radius ratio. Unlike other commonly used separation techniques, free flow based techniques are performed in the liquid phase without the presence of any support matrix, which ensures that the separation occurs under native conditions and at a high recovery rate. Furthermore, the movement of analyte molecules under free flow can inherently be significantly faster than in a porous medium. As such, free flow based separation techniques can enable much faster separation than approaches that employ solid media to keep the analyte molecules confined, such as liquid chromatography or gel electrophoresis. This enhanced separation speed allows free flow based separation techniques to be used for

analysing samples in real-time and for probing processes with dissociation constants faster than the separation speeds of conventional chromatography based techniques.

Microscale versions of free flow electrophoresis are attractive for analytical purposes because of their very fast separation speed of the order of seconds, ability to work with small sample volumes and large surface area to volume ratios of the microscale channels facilitating rapid heat transfer and minimising the detrimental effects of Joule heating even at high voltages. The number of componenents that these setups can simultaneously separate, however, is limited by the broadening of the analyte beams when the molecules migrate in the electric field. This broadening effect originates from diffusive and hydrodynamic as well as electrodynamic and electrohydrodynamic contributions.[10,11] Whereas approaches, such as the application of dynamic coating on the walls of the separation chamber[12,13] and adjusting the conductance between sample and background buffer[14] have been effective in reducing the electrodynamic and electrohydrodynamic distortion effects, respectively, strategies that would simultaneously eliminate the two factors that contribute towards the broadening of the beams as a consequence of the fluid flow - diffusive and hydrodynamic broadening - have been challenging to devise. Indeed, the former of these effects appears due to the random diffusional movement of the analyte molecules and could be in principle alleviated by increasing the fluid flow rate and thus the residence time of the analyte molecules in the separation chamber. The latter contribution, however, arises from the parabolic velocity profile along the height of the separation chamber with effectively zero flow near the walls of the chamber due to non-slip boundary condition (Figure 1a, inset)[10,11] - this leads to a variation in the times that different analyte molecules spend in the separation area and hence to their differential deflection (Figure 1a). In contrast to the diffusive broadening, this effect becomes particularly pronounced when high sample processivity is required[11,15] - increasing the flow rates of the sample and carrier fluid leads to an elevated pressure drop between the inlet and the outlet of the device and hence, according to the Hagen-Poisseuille law, to an increased velocity gradient and elevated variations in the residence times of the analyte molecules. As

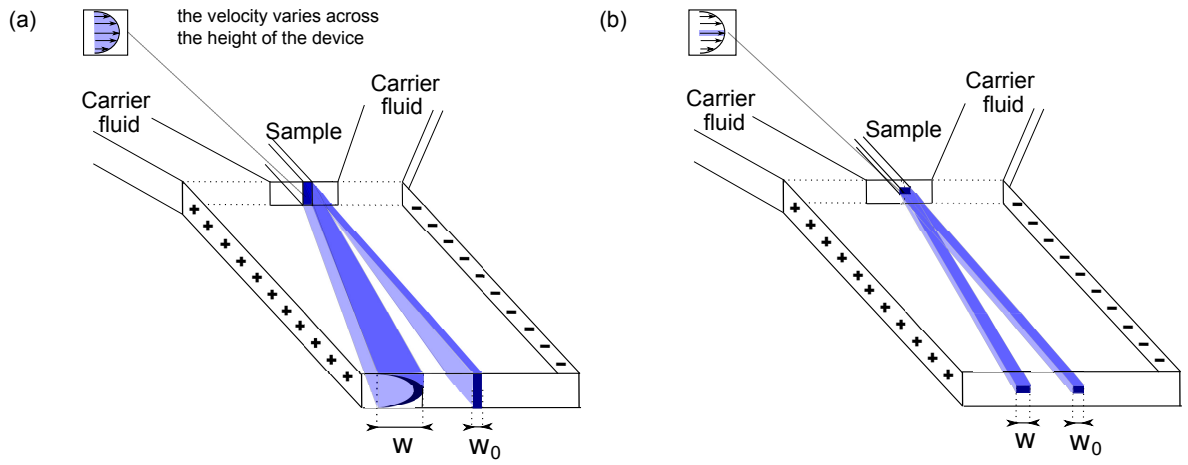

Figure 1: Broadening in free flow electrophoresis devices. **(a)** Pressure difference between the inlet and the outlet of the separation chamber leads to a parabolic velocity profile along the height of the chamber with nearly zero velocity in the vicinity of its walls (inset). This leads to a variation in the times different analyte molecules spend in the device and thus to the broadening of the analyte beam from its original width at no deflection, w_0, to a larger width, w, when the molecules are deflected, substantially limiting the resolution of the separation process. **(b)** This effect can be alleviated by selectively injecting the sample to the areas where velocity gradient and hence the variations in the times that different molecules spend in the separation area are the smallest, minimising the differences in their deflections.

such, the fast flow rates that would on the one hand suppress the diffusive broadening extent, on the other hand lead to an elevated hydrodynamic broadening contribution. Additionally, interval sample injection has been used to suppress hydrodynamic broadening and through this the overall beam broadening effect in free flow electrophoresis setups.[16] However, its implementation led to a discontinuous operation mode, eliminating one of the key advantages of continuous separation techniques.

Here we describe microscale free flow electrophoresis devices, where hydrodynamic broadening is supressed by spatially restricting the injection of the sample only into those areas of the separation chamber where the variations in the velocity are the smallest (Figure 1b).[17] To test the theoretical enhancement in resolution that could be achieved using such a controlled injection strategy we simulated the movement of individual particles - their diffusive and advective transport in combination with their movement in a simultaneously applied electric

field - and showed that a substantial reduction in the broadening of the analyte beam is possible compared to geometries where the sample is injected across the full height of the device. We confirmed that a further enhancement can be achieved by also restricting the sample collection to the central areas only. In particular, we showed that by using a combination of spatially controlled injection and collection, it becomes possible to eliminate almost all beam broadening effect conventionally observed in microscale free flow electrophoresis devices, assuming that the relevant strategies are in place to mitigate electrodynamic broadening effects and contributions related to Joule heating.[10,11]

Spatially controlled injection of samples has been achieved in macro-scale free flow electrophoresis by utilising a narrow plastic capillary tube penetrating into the chamber and bent in the direction of flow.[18] To implement spatial control in a scalable manner in microscale setups and evaluate the predicted enhancement in the resolution experimentally, we used multilayer lithography approaches involving the bonding of two independently produced patterned polymer slabs to one another to generate an orifice which would restrict the sample injection as described. As such a fabrication approach would normally result in microfluidic channels being embedded inside a polymer matrix we further integrated observation windows with the devices to enable high detection sensitivities even in the excitation ranges where the materials used for microfluidic chip fabrication exhibit strong autofluorescence and the molecules inside the polymer could not be detected. With these lithographically produced devices the sheath flow regime is established at the moment when the sample enters the separation chamber and the electric field. Furthermore, the carrier fluid can surround the sample at a range of geometries which is not the case for an inserted capillary where the fluid always surrounds the sample instantaneously in a sheath flow mode. Last but not least, integrating central injection and collection simultaneously with their positions aligned with each another would be extremely challenging to achieve with strategies that rely on the accurate placement of external components such as capillaries, but their simultaneous implementation involves no additional complications when the devices are produced from

lithographically fabricated polymer slabs. With all their structures defined lithographically the devices described in this work can be produced in a straightforward, reproducible and readily scalable manner.

Materials and Methods

Simulating particle movement in microscale channels

The movement of the particles in the micron scale channels both while they were injected or collected over the full height of the device and while their injection and collection were restricted to the central fractions of the channel only, was simulated using Langevin dynamics codes written in C^{++}.[19] Specifically, all the simulations were carried out with a total of $N = 2 \cdot 10^6$ molecules and with reflective boundary conditions at the device walls. The following equations were used to simulate the movement of the k$^{\text{th}}$ particle in the separation area:

$$x_k^{(i+1)} = x_k^{(i)} + v_x(y_k^{(i)},\ z_k^{(i)}) \cdot\ \Delta t + \sqrt{2D\Delta t} \cdot \text{Random}\{-1, +1\} \tag{1}$$

$$y_k^{(i+1)} = y_k^{(i)} + \sqrt{2D\Delta t} \cdot \text{Random}\{-1, +1\} + \mu \cdot E \cdot \Delta t \tag{2}$$

$$z_k^{(i+1)} = z_k^{(i)} + \sqrt{2D\Delta t} \cdot \text{Random}\{-1, +1\}, \tag{3}$$

where the x-axis is in the direction of the length of the channel, y-axis in the direction of its width, z-axis along is height and v_x is the advective flux velocity in x-direction, Δt is the time internal for the simulations, D is the diffusion coefficient of the analyte, μ is its electrophoretic mobility and E the strength of the electric field in the channel. In order to predict the profiles at a specific position along the channel the particle movement was simulated to the point of interest along the length of the channel and the distributions along the y-axis plotted by either averaging the particle distributions along the entirety of the z-axis (full collection) or along a section of interest only (central collection).

Fabrication of two-dimensional microfluidic devices

The replica mould for the two-dimensional (2D) microfluidic devices was fabricated through a single, standard soft-lithography step[20,21] by spinning SU-8 3050 (MicroChem Corp.) photoresist onto a polished silicon wafer to a height of 50 μm and using a custom-built LED-based apparatus for performing the UV exposure step.[22] The mould was used to generate poly(dimethylsiloxane) (PDMS; Dow Corning) based chips and the channels were sealed with a quartz slide (Alfa Aesar, 76.2 x 25.4 x 1.0 mm) after the surface had been activated through oxygen plasma (Diener electronic; 40% power for 15 seconds). The chips were exposed to an additional plasma oxidation step (80% power for 500 seconds) to render the channel surfaces more hydrophilic.[23]

Fabrication of three-dimensional devices with observation areas for enhanced fluorescence detection limit

Three-dimensional (3D) microfluidic devices with observation areas for detection were generated by plasma bonding two individual PDMS chips to each other with one being produced from a multilayer (ML) replica mould and converted to a PDMS chip via standard photolithography approaches similarly to the 2D devices and the other one from a singlelayer (SL) replica mould and converted into PDMS chips with the integration of a non-PDMS based observation window (Figure 4a). Specifically, the mould for the SL chips was fabricated to a height of 50 μm and included all the structures of the device with the exception of the protein inlet and the "bridges" connecting the electrophoresis chamber and the electrolyte channels. The fabrication of the ML replica mould involved two subsequent UV-lithography steps performed with SU-8 3005 and 3050 to obtain 5 μm and 50 μm high channels, respectively. The protein inlet as well as the connecting "bridges" featured only on the 5 μm layer whereas the buffer inlet, the electrophoresis chamber and the electrolyte channels were fabricated onto the 50 μm layer only and identically to how they appeared on the SL replica mould.

Alignment between the two lithography processes was achieved through a custom-built mask aligner including an xyz and a rotating stage (ThorLabs, MBT602/M and PR01/M).

The ML replica mould was converted into a PDMS chip by conventional soft-photolithography approaches as described for the 2D devices (Figure 4a, top). To integrate non-PDMS based observation windows with the SL PDMS chip, small pieces of quartz (ca. 5 mm $\times$ 5 mm) cut out from a 1 mm thick quartz slide (Alfa Aesar) were placed on top of the SU-8 structures of the replica mould in the areas where the imaging was due to take place (Figure 4a, bottom). The quartz pieces were carefully pressed against the SU-8 structures not to destroy the master mould but to ensure that as little PDMS as possible remained between the quartz and the SU-8 structures. The PDMS was then cured by heating it at 65°C for 2 hours - longer baking times were found to cause strong adhesion of the quartz to the SU-8 structures. The PDMS doped with quartz was then carefully pealed off from the SU-8 mould and the PDMS layer above the quartz slide removed with a scalpel to generate a non-PDMS based area for imaging. Inlets for fluidic connections were introduced to the ML PDMS chip using 0.75 mm inner diameter reusable biopsy punch (World Precision Instruments), no ports were introduced to the SL PDMS-quartz chip as it faced downwards during the imaging.

Finally, the SL PDMS-quartz chip was bonded to the ML PDMS chip to form a 3D device. To achieve an alignment accuracy of the order of micrometers between the two chips, drops of water were sprayed onto the two plasma activated chips before they were aligned under a stereomicroscope (4.5x magnification) and then placed in an oven at 65°C for one hour to allow evaporation of the water and the covalent bonding to take place as described earlier.[24] Similarly to the 2D devices, the 3D chips were then exposed to an additional plasma oxidation step (80% power for 500 seconds) to render the channel surfaces more hydrophilic and to aid their priming with the aqueous buffer.

3D devices with no observation windows integrated were produced for comparison analogously to as described above but with no quartz integrated with the SL PDMS chip.

Sample preparation

Bovine serum albumin (BSA) was purchased from Sigma Aldrich and used without further purification. The molecules were dissolved in 10 mM sodium phosphate buffer pH 7.4 to a concentration of 10 mg mL^{-1} for devices that were imaged via PDMS (3D devices with no quartz observation window) and to a concentration of 3 mg mL^{-1} for devices that were imaged through quartz (2D devices and 3D devices with quartz observation window).

Optical detection in the deep UV-wavelength region

The movement of the protein molecules in the microfluidic chips was visualised using a home-built inverted deep-UV fluorescence microscope to exploit the intrinsic fluorescence of aromatic residues of proteins in the deep-UV wavelength range.[25] Briefly, the sample was illuminated using a 30 mW 280 nm LED (Thorlabs) and the light passed through an aspherical lens of a focal length of 20 mm to collimate the beam, and after this onto a dichroic filter cube (280/20-25 nm excitation, 357/44-25 nm emission, 310 nm dichroic beamsplitter). The reflected light from the dichroic mirror was focused onto the sample by an infinity corrected UV objective lens (Thorlabs LMU-10X-UVB; numerical aperture of NA=0.25) and the emitted light collected through the same objective, passed through the emission filter and focused onto an EMCCD camera (Rolera EM-C2). All the used optical components were made out of fused silica to enable high transmission at UV wavelengths.

Results and Discussion

Simulations on the broadening effect in 2D and 3D free flow electrophoresis devices

We modelled the behaviour of the particles in a 50 μm high, 1400 μm wide and 5000 μm long rectangular channel at flow rates of 200, 800 and 2000 μL h^{-1} for a representative protein molecule with a diffusion coefficient of $D = 7 \cdot 10^{-11}$ m^2 s^{-1} (hydrodynamic radius of $R_h = 3.0$ nm) and electrophoretic mobility of $\mu = 2 \cdot 10^{-8}$ m^2 s^{-1} V^{-1} (typical of a protein with isoelectric point in the range of 4-6 under physiological pH - around a third of the proteins in the human proteome are predicted to have their isoelectric point values in that range[26,27]). Under these conditions the Péclet numbers - defined by the ratio of the diffusive time scale in the z-direction and the advective time scale in the x-direction - are Pe = 5.6, Pe = 22, Pe = 56, respectively.

We first modelled the movement of the particles in the electric field when the sample was injected over the full height of the device and noted that there were significant variations in the distribution of the analyte molecules across the height of the chamber at the device outlet (Figure 2a). Specifically, the molecules were more spread in the layers that were further away from the centre (purple line - layers within 0-10% of the total height of the device away from the wall; red line - layers within 20-30% of the total height away from the wall) than in the central layers (green line - layers within 45-55% of the total height away from the wall; all profiles were normalised by the total number of molecules in that layer; simulations were performed at Péclet number of Pe = 22). Indeed, at this relatively high Péclet number the diffusive time scale along the z-axis of the device is significantly longer than the advective timescale along the x-axis and as such, the majority of the molecules that are in the central layers of the device at the end of the channel had been there throughout the time period they moved in the electric field. The tail in the distribution even in the central layers (Figure 2a, green line) compared to the profile with no field applied (blue line)

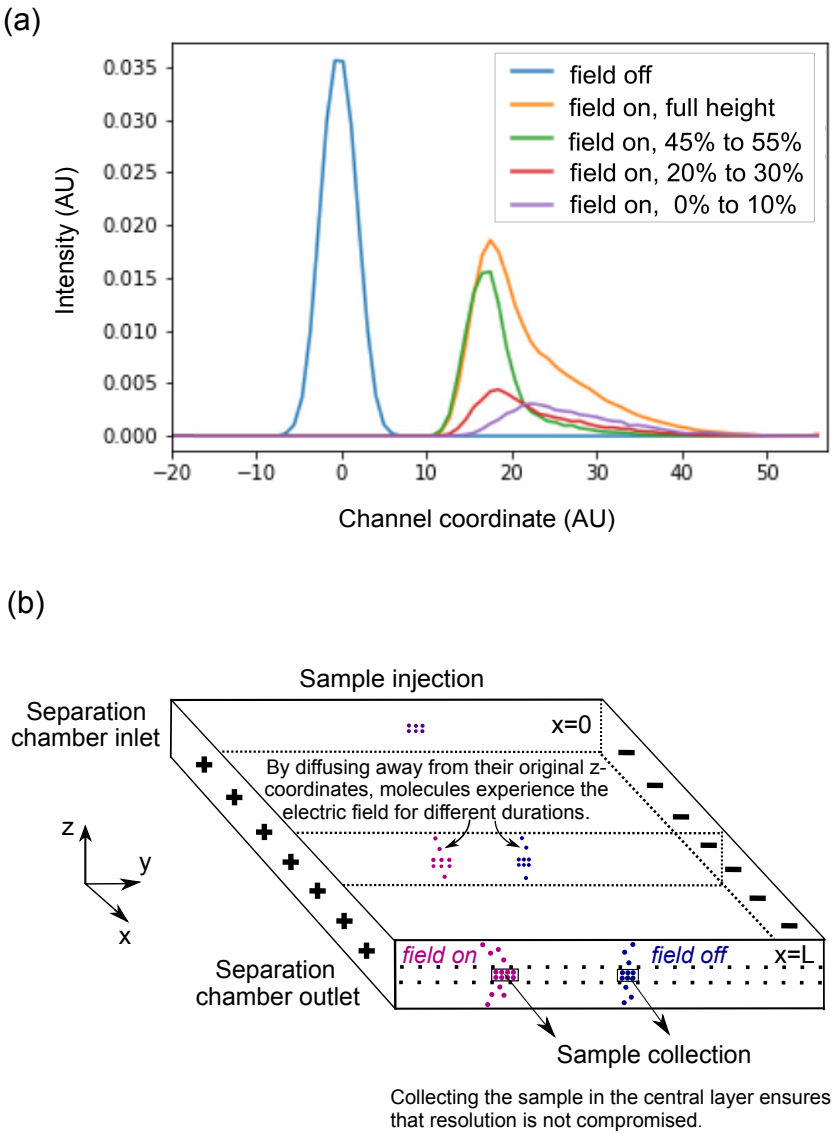

Figure 2: Motivation for spatially controlled collection in free flow electrophoresis. **(a)** By simulating the movement of the analyte molecules in the electrophoresis chamber we observed the analyte beam being substantially more spread in the layers that are further away from the centre (purple line - layers within 0-10% of the total height of the device away from the wall; red line - layers within 20-30% of the total height away from the wall) than in the central layer (green line - layers within 45-55% of the total height away from the wall). The blue line and orange lines correspond to the profiles of the analyte molecules averaged across the full height of the device with and without any electric field applied, respectively. The simulations were performed at Péclet number of Pe = 22 with molecules injected over the full height of the devices. All the shown profiles were normalised by the total number of particles in these layers. **(b)** Based on this variation in the profiles we propose that a further reduction in the broadening of the analyte beam could be achieved by selectively collecting the sample in the central area only.

originated from the small fraction of particles that diffused away from the central layers but also diffused back to these layers.

The data in Figure 2a suggest that a further enhancement in the resolution could be achieved by collecting the sample in the central layers only (Figure 2b). We explored this effect by modelling the behaviour of the particles in the electrophoresis chamber with no electric field applied (Figure 3a-c, red line) and with electric field applied while injecting the sample over the full height of the device (green line), while injecting the sample into the layers within the central 10% of the height of the device (blue line) and while further collecting the centrally injected sample only in the layers within the central 10% of the device height (purple line). The applied voltage was kept indirectly proportional to flow rate to ensure identical deflection under the different flow rates.

For low Péclet numbers, the differences in the observed profiles are small (Figure 3a). Indeed, under these conditions the time scale for the diffusional movement along the height of the device is comparable to that of the advective movement along the channel length, meaning that a significant fraction of the centrally injected molecules can move away from the position they were injected to and experience a longer residence time. Under these conditions the broadening is predominantly arising from simple diffusive rather than hydrodynamic broadening. In contrast, at high Péclet numbers (Figure 3b-c), the diffusive timescale is significantly longer than the advective one and within the analysis time the molecules stay in the central area where they were injected to such that the variation in their residence times remains minimal. By combining the central injection and collection strategies, almost all the hydrodynamic broadening effect can be suppressed (Figure 3b-c, purple line) with the high flow rate also further suppressing diffusional broadening (Figure 3c, purple line). The central injection and collection are of particular importance under these high Péclet number conditions as the high flow rates and strongly pronounced parabolic velocity profiles lead to an extremely wide width of the analyte beam when neither the injection nor the collection is spatially controlled (Figure 3b-c, green line). Indeed, in conventional free flow

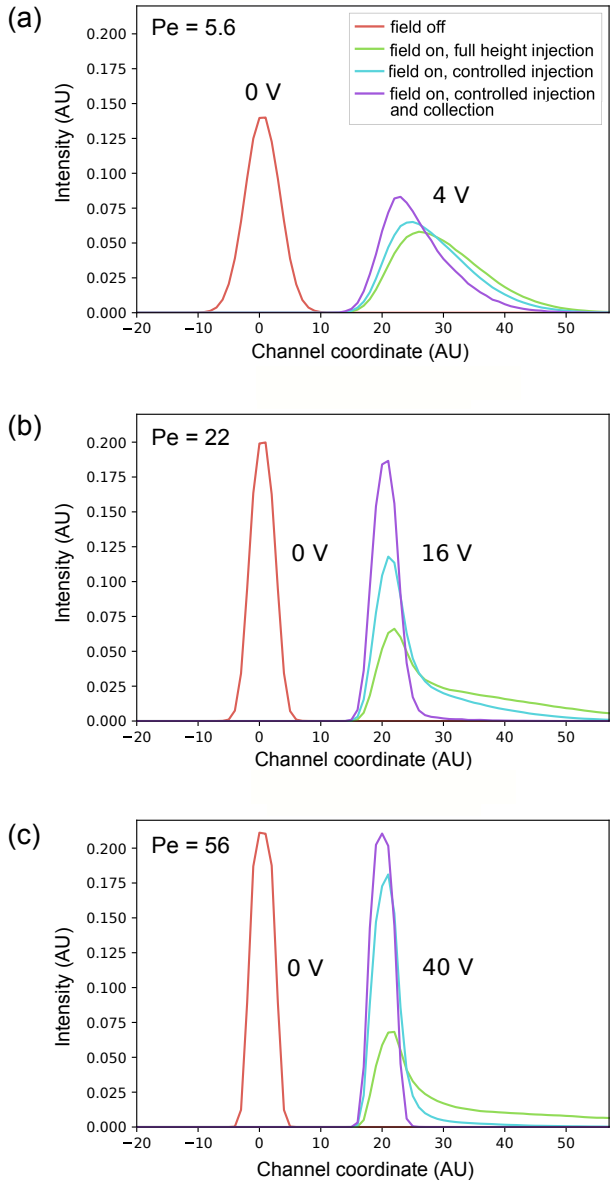

Figure 3: Comparison of the beam broadening effect with spatially controlled and non-controlled sample injection and collection. The profiles were simulated at Péclet numbers of **(a)** Pe = 5.6, **(b)** Pe = 22, and **(c)** Pe = 56, with no electric field applied (red line) and with electric field applied while injecting the sample over the full height of the separation chamber (green line), while injecting the sample to the layers within the central 10% of the height of the device (blue line) and while also collecting the sample only over the layers within the central 10% of the height of the device (purple line). The applied voltage was varied inversely with the flow rate such that the analyte deflection would remain constant between the different flow rates. The simulation results indicated that the reduction in the broadening effect compared to conventional free-flow electrophoretic setups is the most pronounced at the highest Péclet numbers and when both the sample injection and collection are restricted to the central layers only - under these conditions virtually all broadening can be eliminated.

electrophoresis devices, the diffusive broadening effect decreases with increased flow while the hydrodynamic broadening effect decreases with decreased flow and as such, there is an optimum flow rate at which the overall broadening effect can be minised.[9,15] In contrast, for the devices described here both the diffusive and the hydrodynamic broadening contributions decrease with increasing flow rate. This generates the possibility to, in principle, remove all of the broadening effect from these two sources rather than operate the devices under conditions which achieve a compromise between the two effects but do not give the option to simultaneously prevent them.

Experimental performance of the spatially controlled injection for micro free flow electrophoresis

Free flow electrophoresis devices which would facilitate spatially controlled sample injection (3D devices) were produced using multilayer soft-photolitohgraphy approaches - specifically, by bonding multilayer (ML) and singlelayer (SL) microfluidic chips to each other as described in the Materials and Methods section. A major obstacle in producing the 3D devices via previously described multilayered lithography approaches is the requirement to visualise the chip via the polymer that the microfluidic channels are produced in. Indeed, the majority of the polymers used for replicable and scaleable production of microscale devices are either optically non-transparent or exhibit some degree of autofluorescence, therefore generating noticable background signals when the imaging is to take place though them.[28]

In order to circumvent this problem and effectively visualise the movement of the analyte molecules in the microfluidic chips we devised a strategy for integrating an observation hole with the part of the chip which was used for sample visualisation and analysis. Briefly, a quartz slide was placed on top of the lithographically defined structures before the structures were cast in PDMS. This allowed cutting out a section of the PDMS after the two chips had been bonded to one another, such that any excitation and emission would take place through the quartz (Figure 4a). When performing the curing of the PDMS elastomer at optimal

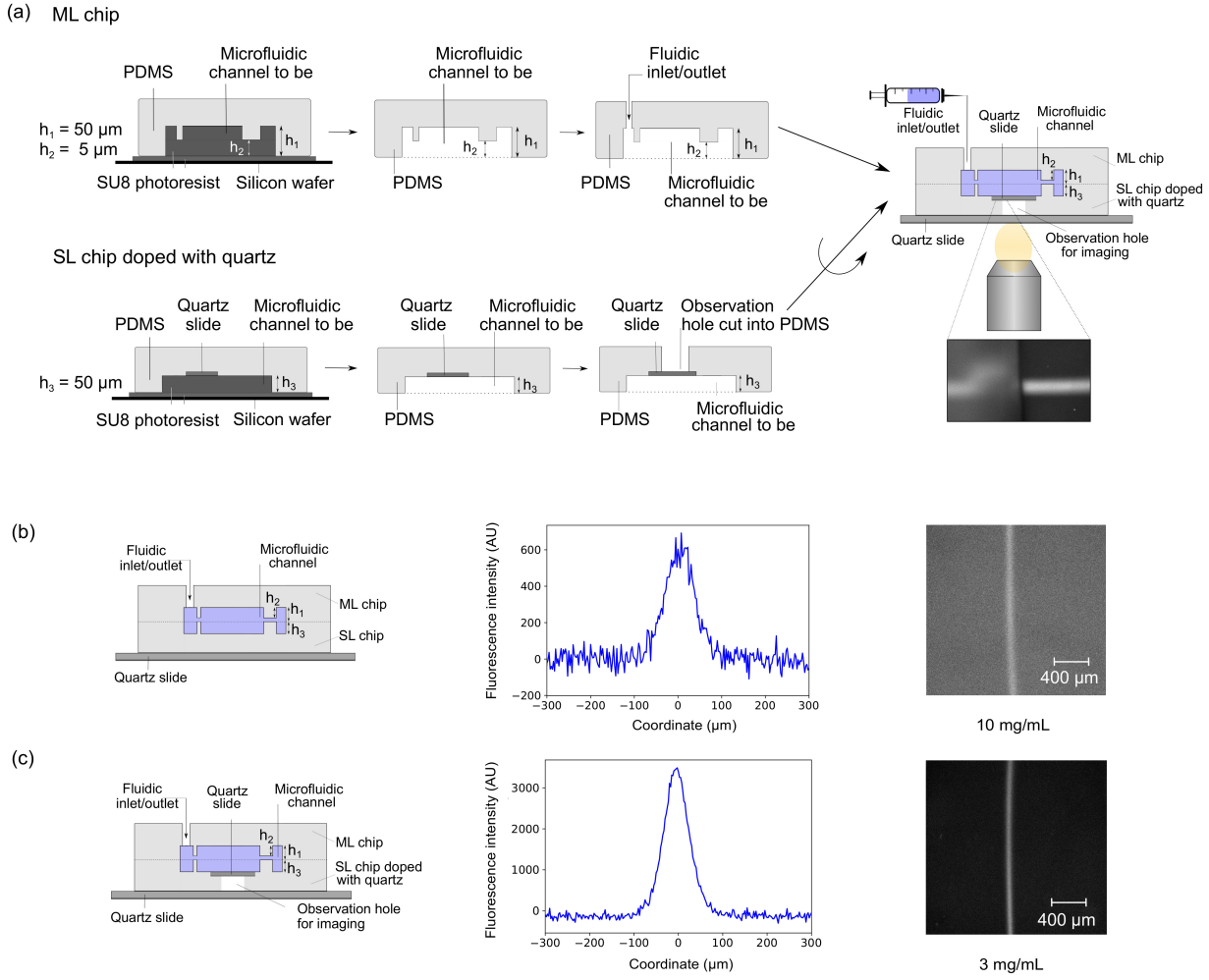

Figure 4: Fabrication of multilayer chips with integrated quartz windows for enhanced fluorescence detection. **(a)** 3D microfluidic devices were fabricated by bonding a multilayer (ML; top row) and a singlelayer (SL; bottom row) chip to one another. A quartz slide was incorporated into the SL chip before curing the PDMS and the PDMS was then removed from the top of the quartz slide with a scalpel in order to introduce a non-PDMS based observation hole for imaging. Fluidic ports were introduced only to the ML chip. The two chips were plasma-bonded to one another and the hybrid 3D chip was imaged via the observation hole fabricated into the PDMS so that the LED light would not need to pass through PDMS for the excitation and the collection of the emitted light. The profile of the sample analyte beam **(b)** in conventional 3D device at 10 mg mL^{-1} and **(c)** in the hybrid 3D device at 3 mg mL^{-1}. The inclusion of the observation window can be seen to substantially enhance the signal to noise ratio.

conditions (Materials and Methods) the quartz-PDMS hybrid slab could be removed from the SU-8 structures without affecting the adhesion of the SU-8 to the silicon wafer, allowing a repeated use of the patterned wafer. Although in principle, the role of the two chips could be reversed with the ML chip including the observation area and the SL chip including the inlets and outlets for sample injection and removal, we decided to fabricate the quartz slide into the SL chip as occasionally the SU-8 structures can come off from the silicon wafer together with the PDMS and the production of SL chips is more straightforward than that of ML chips. When detecting protein analyte molecules in the hybrid PDMS-quartz devices, a significantly enhanced signal to noise ratio was observed compared to those recorded in 3D chips produced through more conventional approaches[21,24] with no observations windows incorporated (Figure 4b,c).

The application of the electric field across the microfluidic separation channel was achieved using a device architecture described earlier.[15] Briefly, the electric potential was applied outside and downstream of the microfluidic separation channel and the field propagated back to the separation area through the use of a co-flowing highly conductive electrolyte solution (Figure 5a). While the narrow fluidic "bridges" between the electrolyte channels and the separation chamber allowed the propagation of the electric field to the separation region of the device, they simultaneously provided a high hydrodynamic resistance to prevent the electrolyte from filling the full separation area and shortcircuit the device but instead permit its slow leakage into the separation chamber and the formation of a stable conductive sheet on the edges of the chamber acting as an electrode. This approach ensures that all the generated electrolysis products, including Joule heat and gaseous products, are flowed away from the chip by the flowing electrolyte solution without ever coming into contact with the analyte. Fabricating connecting "bridges" only on the middle layer (thinner layer of the ML chip mould) where their height is low ensured that with their lengths and widths fixed the "bridges" would have their hydrodynamic resistance maximised but electric resistance minimised.

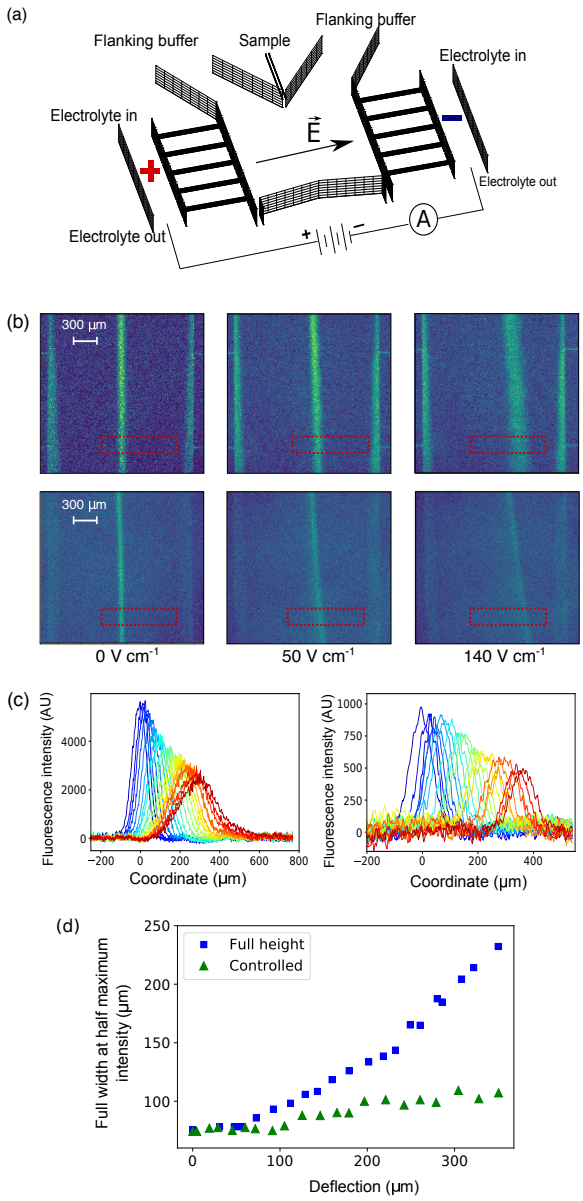

Figure 5: **(a)** The architecture of the microfluidic chip. The sample inlet and the connecting "bridges" between the electrolyte channel and the separation chamber were fabricated onto the thin layer of the ML PDMS chip mould only with the rest of the structures fabricated onto both the thicker layer of the ML PDMS chip mould and the SL PDMS chip mould. **(b)** The profile of the analyte stream for the case when the sample (bovine serum albumin) was injected into the separation chamber across its full height (2D chip; top row) and when its injection was restricted to the central area (3D chip; bottom row). The walls of the electrophoresis chamber are defined by the fluorescent interface on the sides which carries the conductive electrolyte solution. **(c)** The intensity profiles across the red rectangular section shown in panel **(b)** for the 2D (left) and the 3D (right) chip when increasing the field strength linearly from 0 V cm^{-1} (blue) to 140 V cm^{-1} (red). **(d)** The broadening of the analyte stream was observed to be much less significant when the injection was restricted to central areas only - specifically, at the largest deflection studied the relative broadening was found to be around five fold smaller $235\mu m - 75\mu m = 160\mu m$ vs $105\mu m - 75\mu m = 30\mu m$).

The bovine serum albumin (BSA) molecules and buffer were injected into the device via their respective inlets (Figure 5a) at 20 and 380 μL h^{-1} to the 2D devices and at 4 and 800 μL h^{-1} to the 3D devices to yield similar profiles at 0 V cm^{-1} where the beam width is determined by the original sample width and any diffusive broadening that occurs. A voltage ramp from 0 V to 120 V was applied across the devices and the deflection of the BSA molecules recorded by a home-built inverted UV-microscope (Figure 5b) for both chips. The field strength was determined using a calibration strategy as described earlier where an independent estimate was obtained for the resistances of the electrodes by filling the electrophoretic chamber with a highly conductive fluid.[15]

The profiles at different field strength are shown in Figure 5c for the 2D (left) and the 3D (right) devices. To quantify the results, the half-width of analyte beam at its the full-height was used as the parameter to describe the broadening effect. The broadening extent (defined as the difference in the half-width at a specific voltage and at 0 V) was found to be around five times smaller for the devices with restricted injection (Figure 5d green triangles; 150 μm) than for those with non-restricted injection (Figure 5d blue squares; 30 μm) at the maximum deflection studied. We further note that it is possible to reduce the initial width of the analyte beam by adjusting the relative flow rates of the sample solution and the carrier fluid. By doing so, the width of the original beam can be reduced to very small values and in these cases, it is only the broadening extent which determines the effective resolution and the plate number of the separation process. This opens up the possibility to use microfluidic free flow electrophoresis for both, resolving a large number of components from one another and resolving mixtures which include components with very similar electrophoretic mobility values. The strategy of controlling sample injection only to areas where the distributions in the velocity gradients are the smallest can be used to similarly increase the achievable resolutions of separation approaches using strategies other than electric field for the separation, such as magnetic, diffusive or thermal fields.

Conclusions

We have described and demonstrated a microfludic free flow electrophoresis device that allows the injection of the sample to be spatially confined to the central region of the device, thereby simultaneously suppressing the diffusional and hydrodynamic broadening effects encountered in microscale free flow separation setups and, through this spatial control, significantly increasing the achievable resolution. We simulated the movement of the particles in micron scale channels to confirm the suppression of broadening effect and specifically showed that under high Péclet number conditions it becomes possible to eliminate almost all broadening effect encountered in conventional microscale free flow electrophoresis setups. To implement the concept experimentally, we used multilayer soft-photolithography approaches to achieve a precise placement of the components on micron scale and further integrated observation windows with the devices to allow detection in channels that are otherwise embedded inside the polymer. With these devices we showed a five fold reduction in the extent of the broadening of the analyte beam. This improvement opens up the possibility to use microscale free flow separation strategies for resolving complex mixtures with a large number of components as well as separating components with very similar electrophoretic mobilities.

Acknowledgement

The research leading to these results has received funding from the Engineering and Physical Sciences Research Council (K.L.S.) and the European Research Council under the European Union's Seventh Framework Programme (FP7/2007-2013) through the ERC grant PhysProt (agreement n° 337969; T.P.J.K).

Conflict of Interest

Parts of this work have been the subject of a patent application filed by Cambridge Enterprise Limited (GB1720627.7), a fully owned subsidiary of the University of Cambridge.

References

(1) Pamme, N. *Lab Chip* **2007**, *7*, 1644–59.

(2) Turgeon, R. T.; Bowser, M. T. *Anal Bioanal Chem* **2010**, *394*, 187–198.

(3) Janasek, D.; Franzke, J.; Manz, A. *Nature* **2006**, *442*, 374–380.

(4) Kohlheyer, D.; Eijkel, J. C. T.; van den Berg, A.; Schasfoort, R. B. M. *Electrophoresis* **2008**, *29*, 977–993.

(5) Fonslow, B. R.; Barocas, V. H.; Bowser, M. T. *Anal Chem* **2006**, *78*, 5369–5374.

(6) Wen, J.; Wilker, E. W.; Yaffe, M. B.; Jensen, K. F. *Anal Chem* **2010**, *82*, 1253–1260.

(7) Cheng, L.-J.; Chang, H.-C. *Lab Chip* **2014**, 979–987.

(8) Novo, P.; Janasek, D. *Anal Chim Acta* **2017**,

(9) Johnson, A. C.; Bowser, M. T. *Lab Chip* **2018**, *18*, 27–40.

(10) Raymond, D. E.; Manz, A.; Widmer, H. M. *Anal Chem* **1996**, *68*, 2515–2522.

(11) Fonslow, B. R.; Bowser, M. T. *Anal Chem* **2006**, *78*, 8236–8244.

(12) Belder, D.; Ludwig, M. *Electrophoresis* **2003**, *24*, 3595–3606.

(13) Wen, J.; Wilker, E. W.; Yaffe, M. B.; Jensen, K. F. *Anal Chemi* **2010**, *82*, 1253–1260.

(14) Turgeon, R. T.; Bowser, M. T. *Anal and Bioanal Chem* **2009**, *394*, 187–198.

(15) Saar, K. L.; Zhang, Y.; Müller, T.; Kumar, C. P.; Devenish, S.; Lynn, A.; Łapińska, U.; Yang, X.; Linse, S.; Knowles, T. P. *Lab Chip* **2018**, *18*, 162–170.

(16) Shao, J.; Fan, L.-Y.; Cao, C.-X.; Huang, X.-Q.; Xu, Y.-Q. *Electrophoresis* **2012**, *33*, 2065–2074.

(17) Saar, K. L.; Müller, T.; Knowles, T. P. **2017**, GB1720627.7, 11 December 2017.

(18) Weber, G.; Boček, P. *Electrophoresis* **1996**, *17*, 1906–1910.

(19) Müller, T.; Arosio, P.; Rajah, L.; Cohen, S. I.; Yates, E. V.; Vendruscolo, M.; Dobson, C. M.; Knowles, T. P. *Int J Nonlinear Sci* 175–183.

(20) Duffy, D. C.; McDonald, J. C.; Schueller, O. J. A.; Whitesides, G. M. *Anal Chem* **1998**, *70*, 4974–4984.

(21) Qin, D.; Xia, Y.; Whitesides, G. M. *Nat Protoc* **2010**, *5*, 491–502.

(22) Challa, P. K.; Kartanas, T.; Charmet, J.; Knowles, T. P. *Biomicrofluidics* **2017**, *11*, 014113.

(23) Tan, S. H.; Nguyen, N. T.; Chua, Y. C.; Kang, T. G. *Biomicrofluidics* **2010**, *4*, 1–8.

(24) Saar, K.-L.; Yates, E. V.; Müller, T.; Saunier, S.; Dobson, C. M.; Knowles, T. P. *Biophys J* **2016**, *110*, 555–560.

(25) Challa, P. K.; Peter, Q.; Wright, M. A.; Zhang, Y.; Saar, K. L.; Carozza, J. A.; Benesch, J. L.; Knowles, T. P. *Analytical chemistry* **2018**, *90*, 3849–3855.

(26) Wu, S.; Wan, P.; Li, J.; Li, D.; Zhu, Y.; He, F. *Proteomics* **2006**, *6*, 449–455.

(27) Kozlowski, L. P. *Nucleic Acids Res* **2017**, *45*, D1112–D1116.

(28) Piruska, A.; Nikcevic, I.; Lee, S. H.; Ahn, C.; Heineman, W. R.; Limbach, P. A.; Seliskar, C. J. *Lab Chip* **2005**, *5*, 1348–1354.

Graphical TOC Entry